

On the size dependence of cumulus cloud spacing

Thirza van Laar¹ and Roel A J Neggers²

¹Helmholtz-Zentrum Geesthacht

²University of Cologne

November 26, 2022

Abstract

In this study the spatial structure of Trade Wind shallow cumulus populations is investigated as diagnosed from large-domain high resolution cloud-resolving simulations. The main objective is to establish how inter-cloud spacing depends on cloud size, information that is crucial for understanding cloud-radiation interaction and spatial organization, and for informing grey zone parametrizations. A high-resolution cloud-resolving ICON simulation of Caribbean shallow convective cloud fields is used, based on the NARVAL South field campaign. The size statistics of the simulated cloud population are found to compare well to those derived from available satellite images. Four expressions for the nearest neighbor spacing are analyzed, including classic definitions but also novel ones. We find that the dependence of cloud spacing on cloud size strongly depends on this definition. The relation is exponential for the spacing between clouds of similar size, while it is logarithmic for the spacing between clouds of any size. Further analysis suggests that the logarithmic dependence is caused by the abundance of closely-spaced small clouds. The exponential size-dependence is argued to reflect the mesoscale dynamics driving the horizontal size of large convective cells. The implications of the obtained results are briefly discussed.

On the size dependence of cumulus cloud spacing

Thirza W. van Laar^{1*}, Roel A.J. Neggers¹

¹University of Cologne, Institute of Geophysics and Meteorology

Key Points:

- Cloud spacing in Trade wind cumulus populations is investigated using super-large-domain high-resolution simulations
- Various definitions of cloud neighbor spacing are analyzed, including both classic and novel formulations
- Both logarithmic and exponential dependencies on cloud size are reported, reflecting differences in the spatial distribution of small and large clouds

*Current affiliation: Helmholtz-Zentrum Geesthacht, Institute of Coastal Research

Corresponding author: Thirza van Laar, thirza.laar@hzg.de

Abstract

In this study the spatial structure of Trade Wind shallow cumulus populations is investigated as diagnosed from large-domain high resolution cloud-resolving simulations. The main objective is to establish how inter-cloud spacing depends on cloud size, information that is crucial for understanding cloud-radiation interaction and spatial organization, and for informing grey zone parametrizations. A high-resolution cloud-resolving ICON simulation of Caribbean shallow convective cloud fields is used, based on the NARVAL South field campaign. The size statistics of the simulated cloud population are found to compare well to those derived from available satellite images. Four expressions for the nearest neighbor spacing are analyzed, including classic definitions but also novel ones. We find that the dependence of cloud spacing on cloud size strongly depends on this definition. The relation is exponential for the spacing between clouds of similar size, while it is logarithmic for the spacing between clouds of any size. Further analysis suggests that the logarithmic dependence is caused by the abundance of closely-spaced small clouds. The exponential size-dependence is argued to reflect the mesoscale dynamics driving the horizontal size of large convective cells. The implications of the obtained results are briefly discussed.

Plain Language Summary

Shallow cumulus cloud fields persistently cover large areas in the marine subtropics. These low level clouds play an important role in Earth's energy balance, because of the associated vertical transport of heat and moisture and their impact on radiation. Weather and climate models still struggle to correctly represent these cloud populations, which is partially due to our prevailing lack of understanding of their spatial structure. In this study unprecedented large-domain high resolution simulations and satellite images are used to investigate cloud spacing in more detail, revisiting classic studies that were purely based on observational data. The results show that in general cloud spacing increases with cloud size. However, the relation between size and spacing strongly depends on the way the spacing is defined: spacing between clouds of any size behaves logarithmic, while spacing between clouds of equal size shows an exponential size dependence. The results provide more insight into spatial organization of cumulus clouds, and can guide ongoing efforts to improve the representation of these clouds in circulation models.

1 Introduction

Cumuliform low-level clouds persistently cover large areas of the marine subtropics (Norris, 1998). The way these cloud fields interact with the atmospheric circulation and respond to a warming global climate, are complex scientific problems that are not completely understood yet (M. Zhang et al., 2013; Narenpitak et al., 2017). This lack of understanding is reflected in long-standing shortcomings in their representation in weather and climate models (Nam et al., 2012), and in their significant contribution to uncertainty in future climate predictions (Bony & Dufresne, 2005; Sherwood et al., 2014; Vial et al., 2016).

The spatial variability of Trade wind cumulus cloud fields, in particular the spacing between individual cumulus clouds, has been identified as a key element for understanding their role in Earth’s climate system. For example, spatial aggregation is involved in the interaction between cloud fields and a changing climate (Wing & Cronin, 2015; Bretherton & Blossey, 2017; Wing, 2019). The spacing between clouds also strongly affects how they interact with solar and terrestrial radiation, in particular when the three-dimensionality of radiative fluxes is taken into account (Jakub & Mayer, 2017). Cloud spacing also plays a role in the “grey zone problem”, which stands for the situation that previously unresolved convective processes are becoming (partially) resolved at the high resolutions now feasible in general circulation modeling (Wyngaard, 2004; Honnert et al., 2020). While spatial information is needed to make convection schemes scale-aware and scale-adaptive (Neggers, 2015; Brast et al., 2018), cloud spacing also affects the stochasticity in convective properties in the grey zone (Neggers et al., 2019).

Observational research of cloud spacing goes back decades. Early studies mostly relied on high-altitude photography (Plank, 1969), satellite images (Sengupta et al., 1990) and scanning radar (Ali, 1998). Joseph and Cahalan (1990) first investigated the dependence of cloud spacing on cloud size, analysing satellite snapshots of cumulus clouds at various locations on the globe. They reported a positive linear relation between cloud size and the Nearest Neighbor Spacing (NNS), suggesting that larger clouds have a bigger spacing. However, the spread in this relation was large, argued to be due to differences in meteorological and surface conditions between the snapshots. Later studies used the cumulative distribution function of NNS to quantify the spatial organization in a cloud field (Weger et al., 1992; Nair et al., 1998), yielding an organizational metric that has

74 become frequently used (Weger et al., 1993; Tompkins & Semie, 2017). However, the size
75 dependence in cloud spacing has not been revisited since those early days.

76 Large-Eddy Simulations (LES) can well be used to study cloud spacing. A key ad-
77 vantage of LES over satellite images is the access it provides to full four-dimensional fields
78 at high spatial-temporal resolutions. First-generation LES studies of cumulus cloud size
79 distributions were still severely limited by domain size, which made these numerical ex-
80 periments less useful for studying cloud spacing (Neggers et al., 2003). However, ongo-
81 ing advances in supercomputing are currently allowing a dramatic increase in the domain
82 sizes that can be applied (Heinze et al., 2017; Senf et al., 2018; Vial et al., 2019). As a
83 consequence, the simulated cloud populations also become much more complete, which
84 is particularly important for the largest cloud sizes. These large clouds occur more fre-
85 quently and abundantly in a larger domain, and are no longer dynamically constrained
86 in an artificial way by a too small domain size. As a result, the dependence of cloud spac-
87 ing on cloud size can now reliably be investigated with LES across a much broader spec-
88 trum of cloud sizes than was previously possible. While the NNS has appeared in some
89 recent LES studies (Neggers et al., 2019), the unique new opportunities created by the
90 use of a large domain size for studying cloud spacing have not yet been fully exploited.

91 In this study we revisit the classic problem of cloud spacing in Trade Wind cumu-
92 lus cloud fields, now using both super-large domain LES and satellite imagery, in com-
93 bination. Our prime objective is to gain more insight into the dependence of cloud spac-
94 ing on cloud size. Use is made of a high-resolution cloud-resolving simulation performed
95 with the ICON model (Zängl et al., 2014) of Caribbean shallow convective cloud fields
96 as observed during the recent NARVAL-South campaign near Barbados (Klepp et al.,
97 2014). These simulations were generated in the context of the HD(CP)² project (High
98 Definition Clouds and Precipitation for Advancing Climate Prediction). The combina-
99 tion of a large domain ($150 \times 400 \text{ km}^2$) with a cumulus cloud-resolving horizontal res-
100 olution (150 m) allows a statistically significant investigation of cloud spacing across a
101 broad spectrum of cloud sizes, including very large ones. The location over the ocean
102 ensures fairly homogeneous conditions concerning the state of the atmosphere and sur-
103 face characteristics. The simulated cloud populations are compared to statistics derived
104 from MODIS satellite images at 250 m resolution. A set of four definitions of the NNS
105 is examined, including spacing between clouds of any size, spacing between clouds of sim-
106 ilar size, and using both center-to-center and edge-to-edge distancing. The analysis fo-

107 cuses on the dependence of NNS on cloud size. For reference, the obtained results are
108 compared to i) reference NNS values reflecting purely random distributions, and ii) re-
109 sults from the classic observational studies on cloud spacing as mentioned above.

110 The data and methods used in this study are described in Section 2. Section 3 then
111 presents the results, including an assessment of the state of the cloud field and its evo-
112 lution, population statistics and their comparison to observations, and a detailed anal-
113 ysis of the cloud spacing. In Section 4 the main results are further interpreted, focus-
114 ing on the size dependence in the cloud spacing. Section 5 then provides a brief sum-
115 mary of the main results and conclusions, and gives an outlook on future research in-
116 spired by this study.

117 **2 Data and methods**

118 **2.1 20 December 2013**

119 The NARVAL-South Campaign took place throughout December 2013 and Jan-
120 uary 2014 in the Caribbean Trade wind region upwind of Barbados, with the HALO air-
121 craft functioning as the main instrument platform (Klepp et al., 2014). The target area
122 of NARVAL-South is not routinely sampled by state-of-the-art meteorological instrumen-
123 tation, with only a few permanent sites on islands far apart (Stevens et al. 2016, Lamer
124 et al. 2015). Accordingly, NARVAL-South had the aim of filling the existing data gap
125 on Atlantic Trade wind cumulus to support observational data analyses (Schnitt et al.,
126 2017; Jacob et al., 2019) as well as high-resolution simulation efforts (Reilly et al., 2019;
127 Naumann & Kiemle, 2020).

128 The day of interest for this study is 20 December 2013, on which HALO performed
129 Research Flight 08 (RF08). The MODIS Terra satellite image shown in Figure 1a gives
130 a good impression of the cloud field on this day, showing a cumulus cloud population fea-
131 turing a broad range of cloud sizes. Such cloud patterns are typical for the Caribbean
132 Trade wind region (Bony et al., 2020). Figure 1b zooms in on the domain of interest up-
133 wind of Barbados, indicating that in this region the cloud field was dominated by small-
134 scale low level boundary layer cumulus with only a few larger ‘flowers’ present. The lat-
135 ter represent stratiform cumulus outflow near the Trade inversion. The MODIS reflectance
136 is available at 250m gridspacing, which is comparable to the discretization of the LES
137 experiment used in this study.

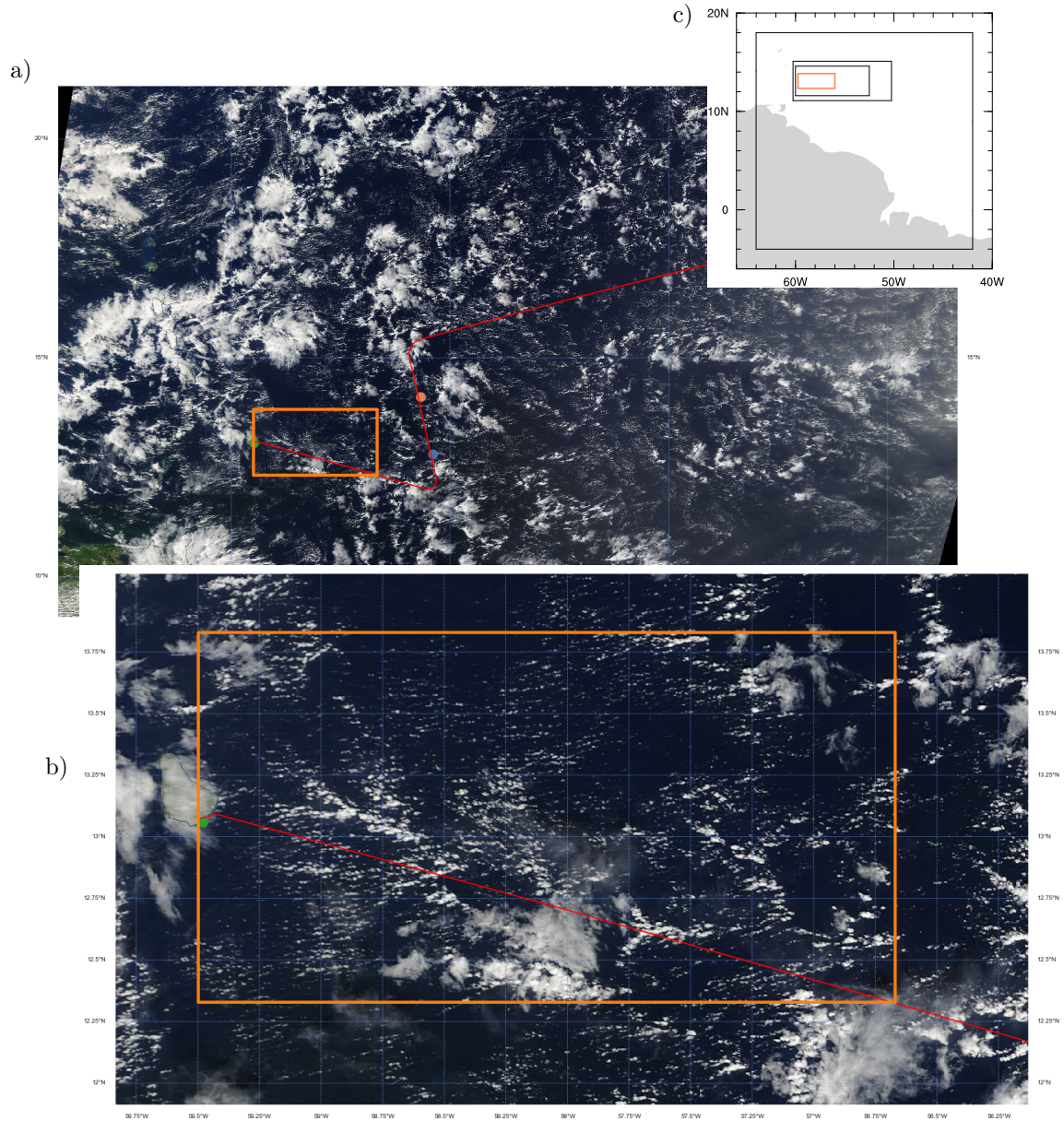


Figure 1. MODIS Terra corrected reflectance (true color) images for 20 December 2013. a) Caribbean at 1km resolution, and b) the area upwind of Barbados at 250m resolution. The Island of Barbados is visible in panel b), on the left. Panel c) gives an overview of all four ICON domains simulated with ICON LES. The orange box always indicates the inner ICON domain resolved at 150m resolution of which the results are used in this study, and within which the MODIS data is also analyzed. The HALO flight path is shown as a red line, while the locations of the first two dropsondes of HALO RF08 are indicated by the blue and orange dots. The Barbados radiosonde sounding is indicated by the green dot. Geotiff data obtained through NASA Worldview (<https://worldview.earthdata.nasa.gov/>).

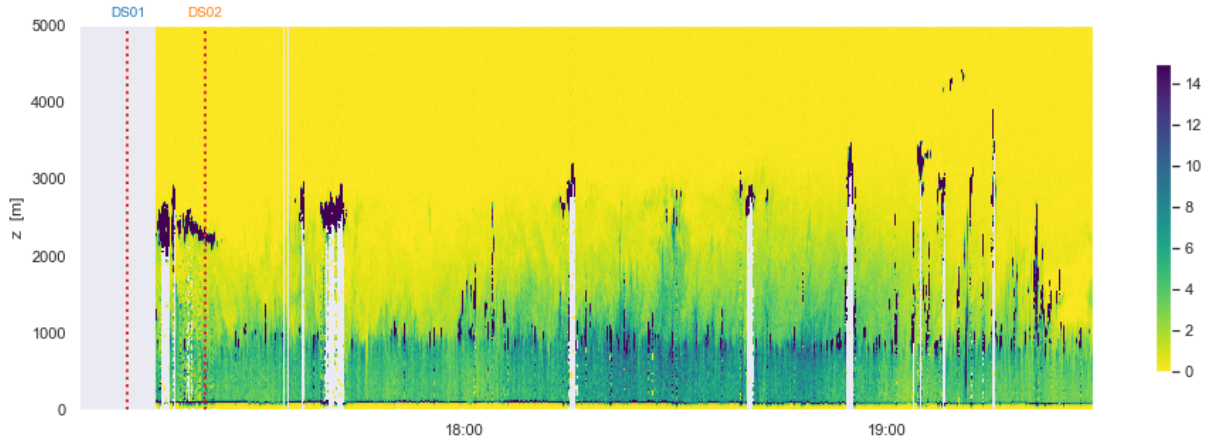


Figure 2. Time-height plot of backscatter at 532 nm as sampled by the HSRL instrument as part of the WALES system onboard HALO during RF08. Only the first part of RF08 is shown during which the observed boundary layer structure was approximately similar. Clouds show up as black areas. Dropsondes DS01 and DS02 are indicated by the dotted red lines.

138 More detailed information about the boundary layer cloud field in the target area
 139 is provided by the WALES instrument onboard HALO, as shown in Fig. 2. Only the first
 140 two-hour time segment of RF08 flight is shown during which defining features of the Trade
 141 wind boundary layer remained relatively unchanged, such as the cloud base and cloud
 142 top heights. After this period HALO entered a region in which the cloud structure deep-
 143 ened profoundly, losing these typical features. This motivated using 19 : 30 UTC as the
 144 upper time limit for the analysis of WALES cloud data. The clouds, showing up as black
 145 areas, are profoundly broken, and include many small cumulus clouds rooting in the sub-
 146 cloud layer as well as remnants of outflow situated below the inversion. These cloud pop-
 147 ulation statistics are similar to those discussed by (Naumann & Kiemle, 2020).

148 Figure 3 shows observed vertical profiles sampled in or in the direct vicinity of the
 149 simulated domain. These locations are also indicated in Fig. 1a. Included are a radiosonde
 150 sounding at Barbados (at 12:00 UTC), the first two dropsondes DS01 and DS02 during
 151 HALO RF08 (launched at 17:12 and 17:23 UTC) just outside the simulated domain in
 152 upwind direction, and the cloud fraction profile as derived from the WALES data dis-
 153 cussed above. The typical features of a shallow cumulus topped Trade wind boundary
 154 layer are evident, such as a well-mixed subcloud layer and a conditionally unstable cloud
 155 layer which is capped by an inversion layer situated between 2200-2600 m height. The

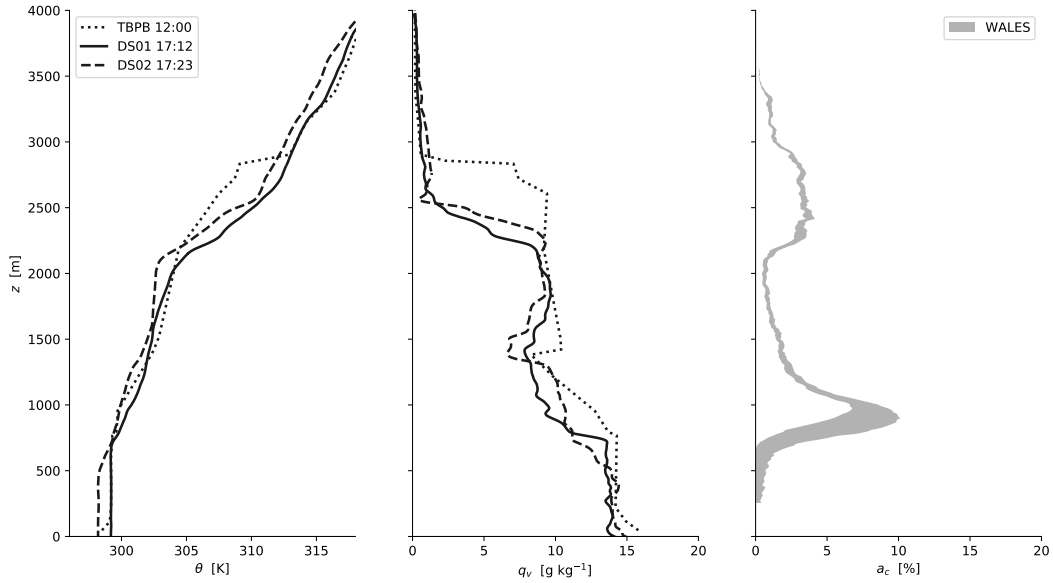


Figure 3. Observed vertical profiles of a) potential temperature θ , b) water vapor specific humidity q_v and c) cloud fraction a_c . Shown are the 12:00 UTC radiosonde sounding from the TBPB station at Barbados (dotted), the first two DropSondes (DS) from HALO RF08 launched at 17:12 (solid) and 17:23 UTC (dashed), and the WALEs HSRL measurements above 250m height and time-averaged over the first two hours of RF08 (shaded grey). The horizontal range for WALEs indicates the difference between the backscatter thresholds of $10 \text{ Mm}^{-1} \text{ sr}^{-1}$ and $20 \text{ Mm}^{-1} \text{ sr}^{-1}$.

156 lower free troposphere above the inversion is statically stable and very dry in all sound-
 157 ings, containing almost no water vapor. The cloud fraction profile shows the double peak
 158 structure typical of Trade wind cumulus as found in numerous previous studies (Stevens
 159 et al., 2001; vanZanten et al., 2011; Nuijens et al., 2014). This structure reflects the pres-
 160 ence of cumuli above the top of the mixed-layer and cumulus outflow near the inversion
 161 as seen in Fig. 2.

162 All thermodynamic soundings are strikingly similar concerning the vertical struc-
 163 ture of the boundary layer, apart from a slightly higher inversion over Barbados which
 164 might be an island effect. This good agreement between soundings that are separated
 165 quite far in both space and time suggests that the boundary layer structure was approx-
 166 imately in steady state as well as reasonably homogeneous across the target domain se-
 167 lected for simulation.

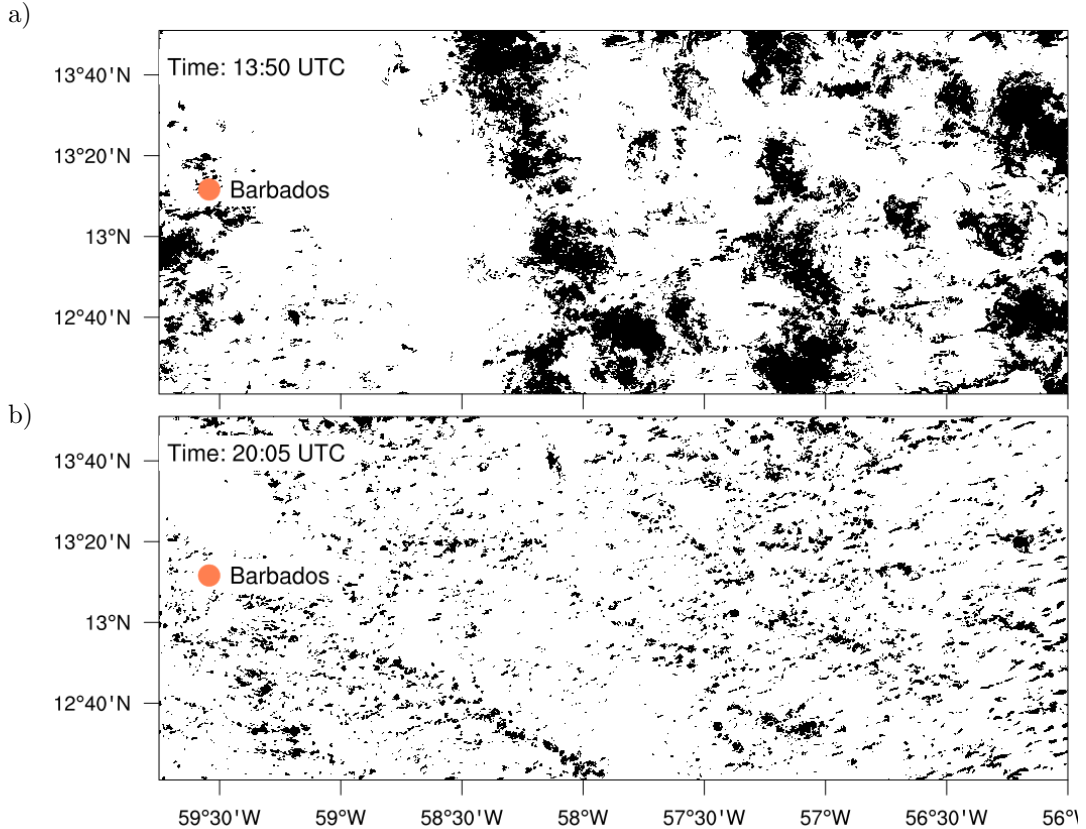


Figure 4. Snapshots of the simulated clouds on 20 December 2013 during the NARVAL-South field campaign. Shown is the cloud mask based on projected liquid water in ICON resolved at 150 m for a) 13:50 UTC and b) 20:05 UTC. Cloudy grid-points are black, while cloud-free points are white. The orange dot shows the location of the island of Barbados.

168 2.2 ICON simulations

169 The simulation data used in this study to investigate the NNS in Trade Wind cu-
 170 mulus were generated in the context of the HD(CP)² project with the Icosahedral Non-
 171 hydrostatic (ICON) model (Zängl et al., 2014; Heinze et al., 2017). At the top of the model
 172 hierarchy are the regional ICON simulations described by Klocke et al. (2017), which con-
 173 sist of a set of four one-way nested domains. At its boundaries the outer domain is forced
 174 by three hourly ECMWF forecast data. Their inner domain, simulated at a 1.2 km hor-
 175 izontal resolution, functioned as the outer domain for the higher resolution LES exper-
 176 iments considered in this study. The configuration of these ICON LES simulations is de-
 177 scribed in detail by the recent studies of Stevens et al. (2019), Vial et al. (2019) and Naumann
 178 and Kiemle (2020), and accordingly only a brief summary will be provided here. Three

179 further nested domain are included, with resolutions of about 600, 300 and 150 m. This
180 yields a total of four domains simulated with LES, as shown in Figure 1c. The inner high-
181 resolution domain (indicated as an orange box) is used in this study for the analysis of
182 cloud spacing. It spans approximately $150 \times 400 \text{ km}^2$ in the horizontal and 21 km in
183 the vertical, discretized at 150 levels (with 30 levels in the lowest 2 km). With a hori-
184 zontal resolution of 150 m the resolution of the inner domain is high enough to switch
185 off all subgrid parametrizations except the ones for the surface layer, turbulence, cloud
186 microphysics (Baldauf et al., 2011), and radiation (Mlawer et al., 1997).

187 The simulation starts at 12 UTC and ends 12 hours later. Every 15 minutes, a 3D
188 field of liquid water is available as output, which serves as input for the clustering al-
189 gorithm (as described in the next subsection). Figure 4 shows snapshots of the cloud mask
190 based on the vertically integrated liquid water at two points in time in the simulation.
191 The domain contains numerous resolved clouds, up to approximately 4500 per snapshot.
192 This sample size, in combination with the broad range of resolved cloud sizes, make these
193 simulations useful for studying spacing between clouds. The surface conditions are rel-
194 atively homogeneous, so that any spatial organization in the cumulus cloud field will be
195 mainly due to large-scale effects or domain-internal dynamics. A simple comparison by
196 eye to the satellite image in Figure 1b suggests that at the later time point the simulated
197 cloud field agrees better with the observed cloud field, lacking the large cloud decks present
198 in the earlier snapshot that likely reflect model spin up effects.

199 A thorough evaluation of LES results against measurements is of crucial importance
200 for gaining confidence in the model and to justify its use for scientific research. This study
201 will make simple comparisons of the simulated boundary layer clouds to the observational
202 data discussed above. In addition, the ICON LES experiments performed for NARVAL-
203 I have already been thoroughly confronted with available observational data in previ-
204 ous studies (Stevens et al., 2019; Vial et al., 2019; Naumann & Kiemle, 2020). This study
205 builds on the encouraging results coming out of these model evaluations concerning the
206 basic state of the trade wind boundary layer. The main focus is then to gain insight into
207 the *two-dimensional spatial statistics* of the simulated cloud population, thus using the
208 simulation as a virtual laboratory. Comparisons of these characteristics will be made be-
209 tween the LES and available satellite imagery. To this purpose a clustering algorithm
210 is used, which is described next.

211 **2.3 Clustering algorithm**

212 A clustering algorithm is used to compute the cloud sizes and locations from out-
 213 put on the model grid. To this purpose the GRIDCLUS algorithm is applied (Schikuta,
 214 1996), which has been used in many LES studies of cumulus cloud fields (Neggers et al.,
 215 2003, 2019; van Laar et al., 2019). The liquid water field is projected on the surface and
 216 a grid cell is considered cloudy if the integrated liquid water path is bigger than the model
 217 threshold of $1 * 10^{-8}$ kg/kg. If two cloudy cells share a cell edge, they are considered
 218 part of the same cloud. Cloud size is defined as the radius of a circle that has the same
 219 area of the cloudy grid cells belonging to the cloud (Rieck et al., 2014). The center of
 220 mass of the cloud is taken as the center of the circle, the coordinates of this point are
 221 used for determining the spacing between the clouds.

222 **2.4 Nearest Neighbor Spacing**

223 The first spacing considered is the distance between a cloud and its closest neigh-
 224 bor, regardless the size of the latter. This distance, hereafter referred to as NNS, is de-
 225 picted in the schematic of Figure 5 together with the other spacings we study. NNS is
 226 calculated following the method adopted from Joseph and Cahalan (1990) and Tompkins
 227 and Semie (2017). In practice this means that for every cloud, the minimum distance
 228 is selected from the distances to all other clouds. Let \mathcal{K} represent the total set of clouds,
 229 with n the total number of clouds: $\mathcal{K} = \{1, 2, \dots, n\}$. NNS between cloud k and its neigh-
 230 bors n is defined as:

$$\text{NNS}(k) = \min\{d(n, k) \mid n \in \mathcal{K} \setminus \{k\}\}, \quad (1)$$

231 with $d(n, k)$ the great circle distance (Euclidian distance corrected for the curvature of
 232 the Earth) between the centers of cloud n and k . The second measure of cloud spacing
 233 that is considered is the distance between a cloud and the closest neighbor that has a
 234 similar size. This measure, referred to as the *equal-size* NNS (NNS_σ), only considers clouds
 235 that have a similar size (l) and belong to the same bin (σ), as determined by the clus-
 236 tering algorithm. This makes our set of clouds dependent on l : $\mathcal{K}_\sigma = \{k \in \mathcal{K} \mid l(k) =$
 237 $\sigma\}$. NNS_σ is then defined as:

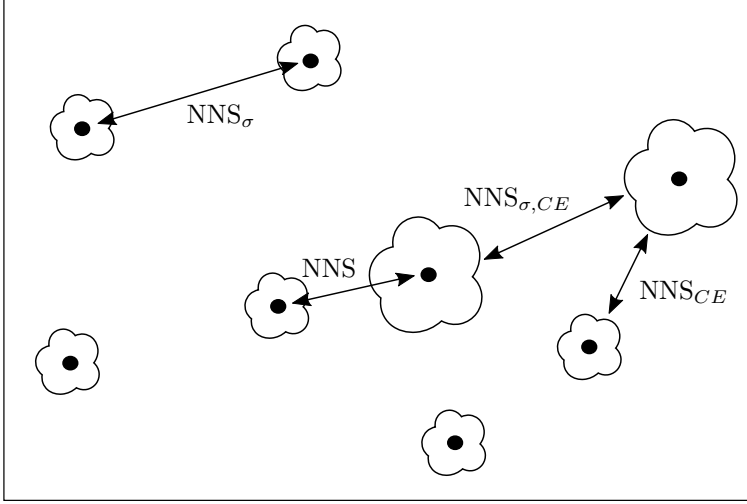


Figure 5. Example field with two cloud sizes showing the difference between NNS (distance between one cloud and its' nearest neighbor) and NNS_σ (distance between one cloud and its' nearest neighbor of a similar size).

$$\text{NNS}_{\sigma}(k) = \min\{d(n, k) \mid n \in \mathcal{K}_{\sigma} \setminus \{k\}\}. \quad (2)$$

238 In calculating NNS and NNS_σ two different approaches were followed, yielding in
 239 total four measures of cloud spacing. First, the *cloud center spacing* is used, the distance
 240 from cloud center to cloud center. Second, the *cloud edge spacing* is the distance from
 241 cloud edge to cloud edge, computed by assuming that all clouds are perfect circles (Rieck
 242 et al., 2014; Dawe & Austin, 2013). In essence, it is the cloud center spacing minus the
 243 size (radius) of the two neighboring clouds: $d_{CE} = d(n, k) - r_n - r_k$. Then the NNS_{CE}
 244 for using cloud edge spacing is defined as:

$$\text{NNS}_{CE}(k) = \min\{d_{CE}(n, k) \mid n \in \mathcal{K} \setminus \{k\}\}, \quad (3)$$

245 and the equal-size NNS using cloud edge spacing ($\text{NNS}_{\sigma,CE}$) as:

$$\text{NNS}_{\sigma,CE}(k) = \min\{d_{CE}(n, k) \mid n \in \mathcal{K}_{\sigma} \setminus \{k\}\}. \quad (4)$$

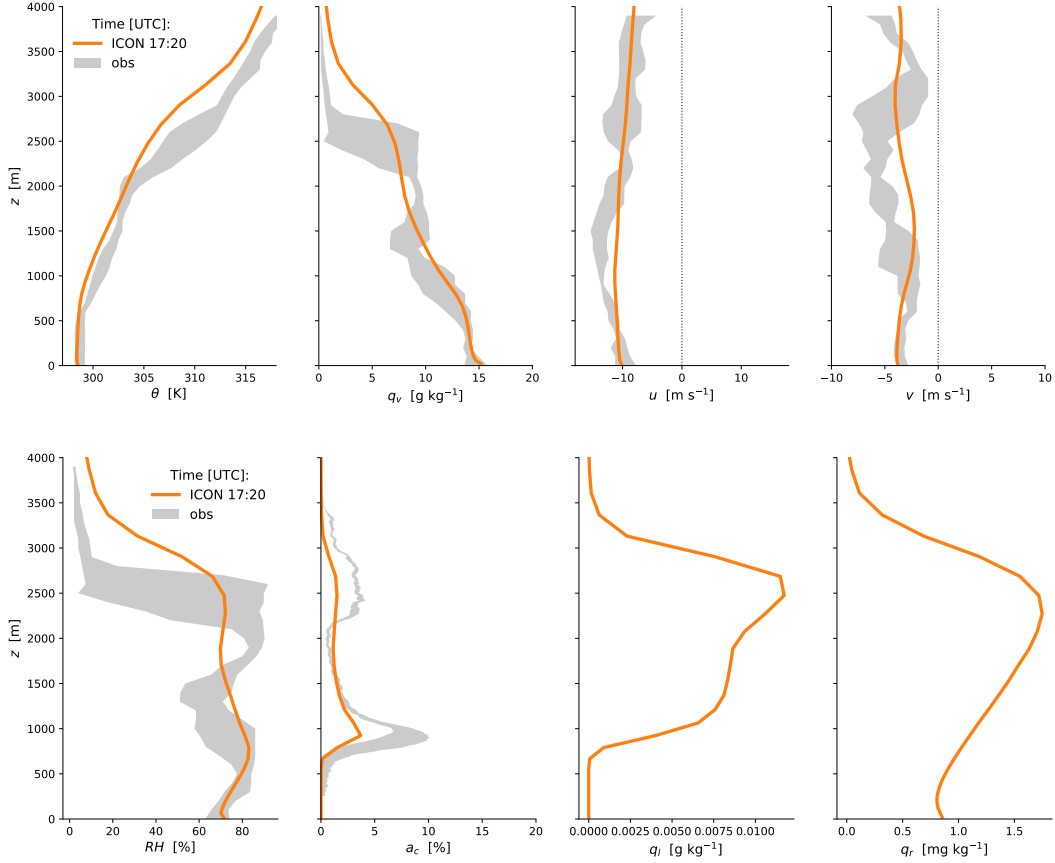


Figure 6. Vertical structure of the simulated (orange) and observed (grey) Trade wind boundary layer during RF08. Shown are a) potential temperature θ , b) water vapor specific humidity q_v , c) zonal wind speed u , d) meridional wind speed v , e) relative humidity RH , f) cloud fraction a_c , g) cloud liquid water q_c and h) rain water q_r . Sonde observations include the first two dropsondes and the Barbados radiosonde, the range indicating the minima and maxima encountered within 100m height bins. The WALES data plotted in f) is identical to those shown in Figure 3c.

246

2.5 Reference NNS values

247

248

249

250

251

252

Previous studies on spatial organization (Zhu et al., 1992; Nair et al., 1998) using cumulative distribution functions have yielded reference values of NNS that reflect purely randomly distributed populations. These reference values are based on a Poisson point process, which is a collection of points randomly distributed in space. The number of points can then be described by a Poisson distribution. When assuming clouds can be represented by points, the cumulative distribution of the nearest neighbor distances of

253 cumulus clouds can be directly compared to the cumulative distribution of distances of
 254 a Poisson point process. The comparison between our simulated field and a random field
 255 can be summarized with a single value, referred to as I_{org} (Organization Index) (Tompkins
 256 & Semie, 2017). I_{org} distinguishes three regimes: randomness ($I_{org} \approx 0.5$), clustering (I_{org}
 257 > 0.5) and regularity ($I_{org} < 0.5$).

258 Based on a Poisson process and following the mathematical derivation, one can also
 259 define the mean NNS a random distribution would give (NNS_{ran}) (Weger et al., 1992):

$$NNS_{ran} = \frac{\sqrt{A}}{2\sqrt{N}}. \quad (5)$$

260 Here A is the domain area and N the number of clouds. As opposed to a random
 261 distribution of clouds one could also think of a regular distribution. In that case the clouds
 262 form a grid-like pattern, thereby maximizing NNS for the given amount of clouds. This
 263 NNS_{reg} could be determined as follows:

$$NNS_{reg} = \sqrt{\left(\frac{A}{N}\right)}. \quad (6)$$

264 **3 Results**

265 **3.1 Vertical structure**

266 Figure 6 shows vertical profiles of variables expressing the vertical structure of the
 267 simulated Trade wind boundary layer. For each variable measurements are included when
 268 available, including the first two dropsondes of HALO RF08, the Barbados radiosonde
 269 and WALES cloud fraction profile as already shown in Figure 3. The simulation data
 270 is sampled at the output timepoint (17:20 UTC) closest to the two dropsondes, and av-
 271 eraged over the full domain in order to optimize comparability with the sounding data
 272 which covers a similar spatial domain. The results suggest that the thermodynamic ver-
 273 tical structure of the cloud layer is reproduced reasonably well by the simulation, with
 274 the subcloud mixed layer and convective cloud layer situated at the right heights and
 275 featuring a similar conditional instability and humidity gradient. Slight thermodynamic
 276 biases include an overestimation in the inversion height and a small cold and moist bias
 277 in the lower free troposphere. The wind structure is realistic, including a well-defined
 278 easterly throughout the lowest 4 km featuring a small northerly component.

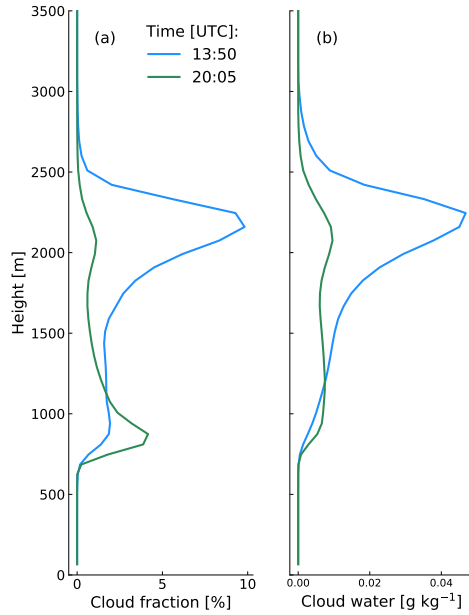


Figure 7. Simulated vertical profiles of a) cloud fraction and b) cloud water averaged over the domain at the two timepoints of the instantaneous cloud fields shown Figure 4. The line colors corresponds to the coloured time points as shown in Figure 8, for reference.

279 Figure 6 (e-f) focuses on the simulated cloud structure. Defining and typical Trade
 280 wind cloud features that are reproduced include the two distinct maxima in relative hu-
 281 midity at approximately ~ 700 m and ~ 2500 m height, and a concave structure sit-
 282 uated in between. This structure and amplitude agrees well with the observations. A sim-
 283 ilar two-mode structure is evident in the cloud fraction profile, reproducing the WALES
 284 observations in this respect. The model slightly underestimates the magnitude of the pro-
 285 file at these two maxima, for which we speculate two reasons can exist; i) the threshold
 286 value range used to compute the observed profile from backscatter measurements, or ii)
 287 a lack of skill in LES to produce enough cloud mass. The latter would be consistent with
 288 results reported in recent studies comparing LES results to cloud observations (Y. Zhang
 289 et al., 2017). More research is required to gain insight into this question. For cloud liq-
 290 uid and rain water no observations are available; however, their vertical structure is sim-
 291 ilar to LES results for previous Caribbean cumulus cases (vanZanten et al., 2011).

292 Despite slight biases, the overall assessment is that the key features of the Trade
 293 wind boundary layer observed in the region during RF08 are reproduced to a high enough

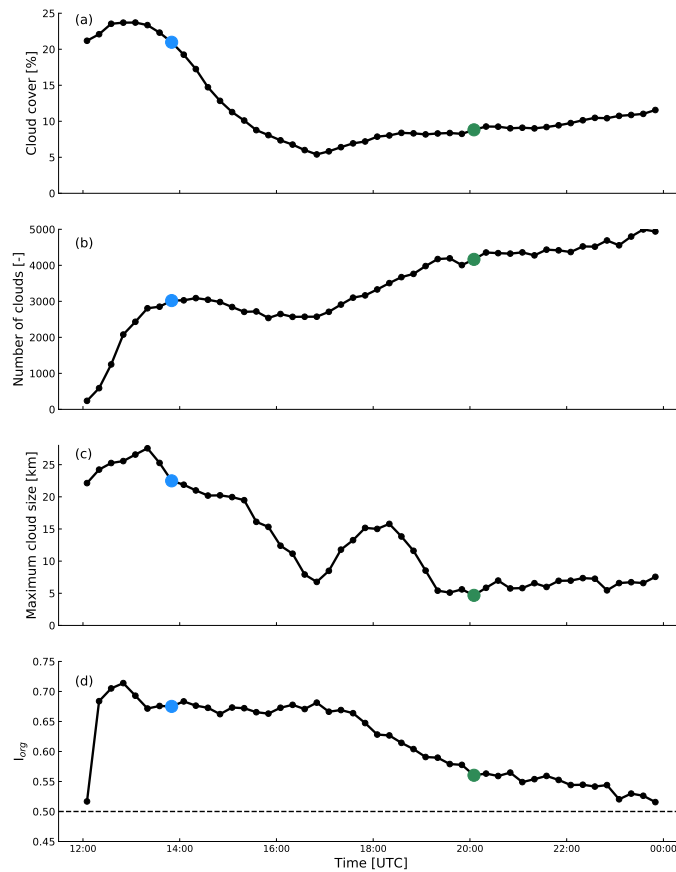


Figure 8. Timeseries of a) cloud cover, b) number of clouds, c) maximum cloud size and d) I_{org} . The blue and green dot correspond to the upper and lower panel of Figure 4 respectively.

294 degree to justify using this simulation for further investigation of cumulus cloud spac-
 295 ing.

296 **3.2 Time evolution**

297 While the good agreement with the observed vertical structure of the boundary layer
 298 during RF08 is encouraging, it is important to realize that this evaluation only applies
 299 to a brief time-window. In fact, Figure 4 already demonstrated that the spatial struc-
 300 ture of the simulated cloud field experiences a substantial transition in time. Figure 7
 301 further shows that the transition not only concerns the spatial structure but also the cloud
 302 vertical structure, here diagnosed at the exact two snapshots as shown in Figure 4. The
 303 first phase should be considered model spin-up, as it is still close to the initialization time
 304 of the simulation. This phase is characterized by high cloud covers and high cloud wa-

305 ter amounts at a height slightly above 2 km, formed by large cumulus outflow clouds.
306 The large clouds are not numerous, but do have sizes up to approximately 25 km. In con-
307 trast, later in the simulation the distribution is dominated by many more smaller clouds,
308 and has far less large outflow cloud layers.

309 The transition of the cloud field is perhaps best expressed by the timeseries of cloud
310 cover, clouds number and maximum cloud size as shown in Figure 8a-c. During the first
311 two hours of the simulation the number of clouds rapidly increases; subsequently the in-
312 crease is much more gradual. The latter phase is accompanied by a drop in cloud cover
313 and maximum cloud size. This combination indicates that the initial large structures are
314 gradually being replaced by smaller clouds. The increase in cloud number mainly hap-
315 pens at lower levels, as expressed by the cloud cover similarly increasing in that height
316 range (Figure 7). Low-level clouds become more pronounced as time progresses, although
317 their liquid water content is lower compared to the high-level clouds. The decrease of
318 projected cloud cover over time (Figure 8a) is driven by the disappearance of the high-
319 level clouds. During the second half of the simulation the maximum cloud size stays more
320 or less constant at about 5 km, except for a modest peak around 18:00 UTC.

321 Apart from the transition in cloud cover, number and maximum size, their spatial
322 distribution changes as well. Figure 4 suggests that the large cloud clusters are gradu-
323 ally replaced by smaller clouds that are either randomly distributed or form cloud streets.
324 A quantification of the degree of organization is provided by I_{org} , shown in Figure 8d.
325 The black dashed line in the figure indicates pure randomness, therefore I_{org} suggests
326 strong organization at the beginning of the simulation. The degree of organization starts
327 to decrease around 17:00 UTC, with values close to random at the end of the simula-
328 tion.

329 Based on this analysis of the temporal evolution of the cloud field and the obser-
330 vational data showing a cloud field dominated by small-scale low level boundary layer
331 cumulus, we decided to take the first six hours of the simulation not into account for the
332 analysis. After this period the cloud cover, maximum size and number stay more or less
333 constant. This behavior motivates using only the last six hours (24 time steps) for the
334 analysis of the size distributions of cloud number and cloud spacing.

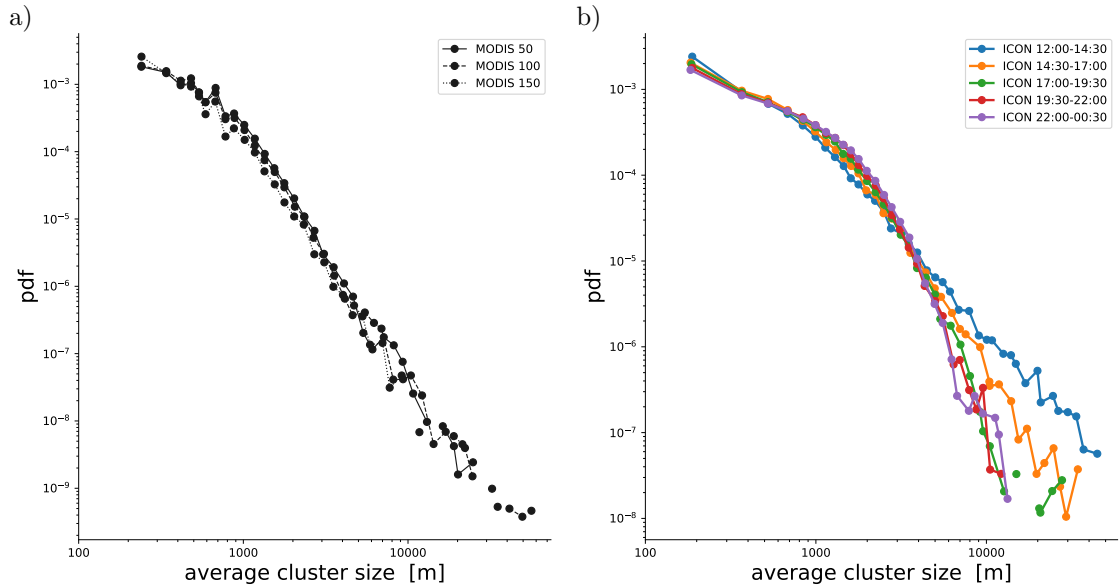


Figure 9. Size distributions of the number of clusters as derived from observations and simulations. a) Based on MODIS satellite image as shown in Figure 1b, showing results for three reflectance thresholds (50, 100 and 150) to define cloudy pixels. b) Distributions diagnosed from the integrated liquid water path in ICON for five subsequent time-periods (indicated by the UTC times in the legend). The vertical axis represents the normalized cluster number divided by the binwidth, while the horizontal axis represents the average cluster size per bin. Log-linear binning is used to calculate these histograms, as described in the text.

335 3.3 Size distributions

336 Figure 9 shows size distributions of the observed and simulated number of clouds.
 337 These CSDs (cloud size distributions) have been generated using the clustering algorithms
 338 as described in Section 2.3. The CSDs for the MODIS image as shown in Figure 1b are
 339 derived using three thresholds for reflectance in the red channel. The clusters are size-
 340 sorted using the linear-logarithmic binning as described by Quinn and Neelin (2017), which
 341 ensures that the binwidth can not be smaller than the smallest possible cluster size. To
 342 this purpose minimum binwidths of 250m and 150 m are used, which are the effective
 343 resolutions of the MODIS product and the LES simulations, respectively.

344 Both the simulated and observed size distributions exhibit a similar functional form
 345 in their dependence on cluster size. This shape, featuring two size-ranges with a distinctly
 346 different size-dependence, has often been reported in previous studies of cumulus con-
 347 vection (Neggers et al., 2003). In both the observations and the simulation the cluster

Table 1. Powerlaw exponents b resulting from least-square fits in log-log space of a single powerlaw function al^b to the size densities shown in Figure 9. Fits are applied in two ranges of cluster sizes l , including a small (0-1 km) and a large (1-10 km) range.

dataset	0 – 1 km	1 – 10 km
MODIS 50	-1.29	-3.88
MODIS 100	-1.48	-3.90
MODIS 150	-2.05	-3.85
ICON 12:00-14:30	-1.24	-2.38
ICON 14:30-17:00	-1.05	-2.82
ICON 17:00-19:30	-0.99	-3.60
ICON 19:30-22:00	-0.89	-3.71
ICON 22:00-00:30	-0.85	-3.96

348 size at which the dependence changes is at about 1km. Applying a single powerlaw fit
 349 in both size ranges yields powerlaw exponents as listed in Table 1. The model reproduces
 350 the distinct difference in powerlaw exponents between the two size-ranges. Note that the
 351 observed CSD shifts to the left with a higher reflectance threshold, expressing that fewer
 352 clusters are then detected, as can be expected. However, the distribution shape is still
 353 preserved. Over time the simulated CSD becomes steeper in the large size range, express-
 354 ing that less and less big structures feature in the simulation.

355 The range of observed cluster sizes spans about three orders of magnitude, with
 356 the largest cluster size being about 60 km. Note that this maximum size does show strong
 357 dependence on the reflectance threshold, reducing to 30 km for the highest value. Ac-
 358 cordingly, this aspect of the distribution is not very robust, also because the sample size
 359 is very small in this tail of the distribution. The simulated maximum cluster size is some-
 360 what lower, but still significantly larger than the scales of moist boundary layer updrafts.
 361 These results reflect that while some larger stratiform outflow clouds do appear in the
 362 simulation, their total number is underestimated. Note that our main goal is to study
 363 spacing among cumuliform clouds, which sit in the left and middle part of the distribu-

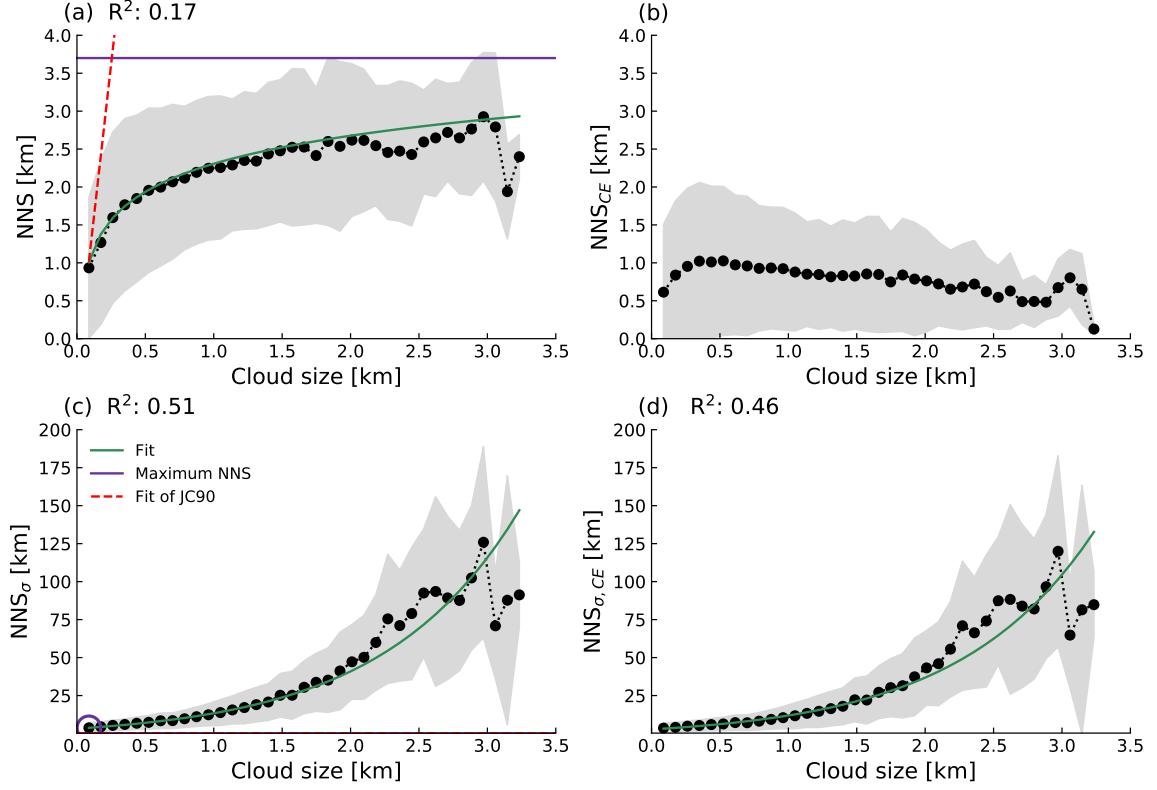


Figure 10. Cloud spacing as a function of cloud size. Shown are a) NNS, b) NNS_{CE} , c) NNS_{σ} , and d) $NNS_{\sigma, CE}$. The NNS is averaged over all analysed fields, the grey area shows the mean \pm the standard deviation. The green lines show the best fits through the data with their R^2 value in the upper left corner. The purple line (a) and circle (c) indicate the maximum NNS and the Red dashed line shows the fit (Joseph & Cahalan, 1990) found.

364 tion. Accordingly, the underestimation of the number of large stratiform cloud decks does
 365 not harm the usefulness of the simulation.

366 We conclude from this comparison that the simulated cloud populations are rep-
 367 resentative of subtropical marine conditions as typically occur in the Trade wind regions,
 368 and of the cumulus cloud population as observed on 20 December 2013 in particular. This
 369 motivates using the simulation output for further analysis of cloud spacing.

370 3.4 Cloud spacing

371 The four panels of Figure 10 show the size dependence for all four definitions of the
 372 Nearest Neighbor Spacing (NNS) as defined in Section 2.4 and as applied to the ICON

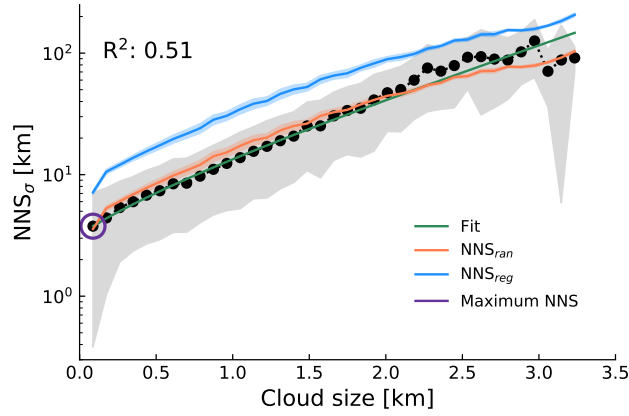


Figure 11. Same as Figure 10c but now showing NNS_{σ} using log-linear axes. Also included are NNS_{ran} and NNS_{reg} , for reference.

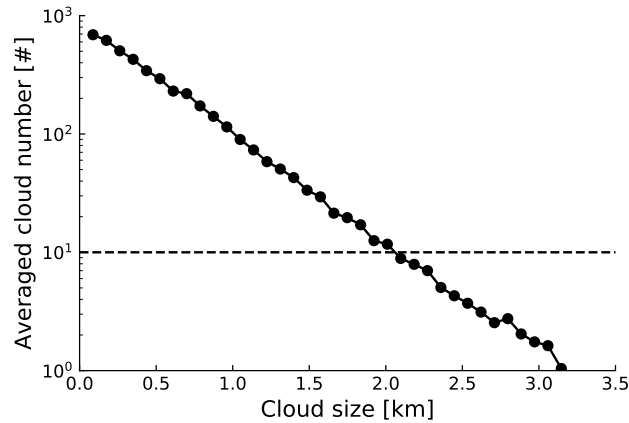


Figure 12. Number of clouds per cloud size, averaged over all snapshots used for analysis. For the calculation of this histogram a constant bin-size is used. The horizontal dashed line refers to the statistical analysis in Section 3.4.

373 LES fields. The results represent averages over the last six hours of the simulation. A
 374 least squares fit is made for the size dependence in each NNS definition, adopting a func-
 375 tional form that yielded the largest R^2 value (proportion of total variance explained by
 376 the fit) for each definition. Unfortunately the limited availability of MODIS data for this
 377 day and area (only a single snapshot) yields a sample size too low to reliably carry out
 378 this cloud spacing analysis for the observational data. Accordingly, this is for now con-
 379 sidered a future research topic.

380 Figure 10a shows the size dependence of NNS, which in the range < 600 m shows
 381 a linear relation, just like the fit reported by Joseph and Cahalan (1990). However, at

382 larger sizes the dependence is best captured by a logarithmic relation ($y = 2.31 + 1.23 \log_{10}(x)$),
 383 with an R^2 value of 0.17. For the larger cloud sizes, the mean falls slightly below the fit.
 384 The limited amount of data for the statistical analysis might be a reason for this; cloud
 385 number decreases strongly with cloud size, so that the largest clouds only rarely occur.
 386 This is well visible in Figure 12 b, in which a dotted line at an average of 10 clouds per
 387 bin is added for reference. The cloud size associated with this sample size is about 2 km;
 388 note that this is also the size above which the NNS starts to deviate significantly from
 389 the proposed fit (see Figure 10a). This suggests that a number of 10 clouds is the min-
 390 imum sample size at which a clear functionality becomes apparent in the size dependence
 391 of the NNS.

392 The spacing between clouds of a similar size, NNS_{σ} (Eq. 2), is shown in Figure 10c.
 393 Again we find a monotonically increasing cloud spacing with cloud size; however, for this
 394 definition the relation is best captured by an exponential function ($y = -2.66 + 5.90 \exp(x)$)
 395 with an R^2 value of 0.51. Other differences with NNS include i) much larger spacing val-
 396 ues across the spectrum and ii) an increasing spread around the mean. The larger spac-
 397 ing of NNS_{σ} in general, as compared to NNS, directly reflects that only a subset of all
 398 clouds in the population is considered when calculating the equal-size spacing; a lower
 399 density of clouds in an area is directly associated with a larger spacing. But the expo-
 400 nential increase with size of the NNS_{σ} is not so trivial, and will be further interpreted
 401 in Section 4.3.

402 It makes sense to compare the equal-size cloud spacing NNS_{σ} to the theoretical lim-
 403 its NNS_{ran} and NNS_{reg} , as defined in section 2.4. The results of this comparison are shown
 404 in Figure 11. NNS_{σ} is very similar to NNS_{ran} ; for all cloud sizes NNS_{ran} stays within
 405 the spread of NNS_{σ} . At the same time NNS_{σ} has significantly lower values than NNS_{reg} .
 406 The spatial distribution of clouds of a given size is close to random, although some dif-
 407 ferences between small and big clouds can be distinguished. The equal-size spacing for
 408 small clouds is slightly smaller than what a random distribution (following a Poisson point
 409 process) would give, meaning that they are more clustered together. NNS_{σ} for larger clouds,
 410 on the other hand, is larger than NNS_{ran} and resembles more a regular distribution.

411 The impact of cloud edge spacing on the NNS is investigated in Figure 10b and d.
 412 When interpreting these results it is important to consider that the spacing for bigger
 413 clouds could be larger simply because their centers are spaced further apart, due to their

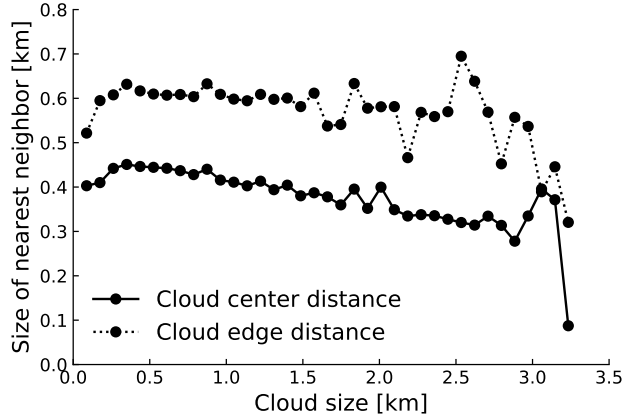


Figure 13. The averaged nearest neighbor size as a function of cloud size, using both the cloud center spacing (solid) and the cloud edge spacing (dotted).

414 size. Spacing definitions NNS_{CE} and $NNS_{\sigma,CE}$, as defined by Equations 3 and 4, both
 415 reflect this effect. Using the cloud edge for the spacing leads to only minor differences
 416 for NNS_{σ} , preserving its functional dependence but shifting it downwards somewhat (Fig-
 417 ure 10d). The exponential again yields the best fit ($y = -2.60 + 5.33 \exp(x)$), albeit
 418 with a slightly lower R^2 value of 0.46. In contrast, for NNS_{CE} (Figure 10b), the spac-
 419 ing is not only smaller, the logarithmic dependence is also lost. After a first increase of
 420 NNS_{CE} with cloud size, for clouds larger than about 400 meter a slight decrease of spac-
 421 ing with size is visible.

422 4 Interpretation

423 4.1 The impact of edge versus center spacing

424 More insight into the strong impact of adopting cloud-edge spacing versus cloud-
 425 center spacing on the size dependence of NNS is provided by considering the size of the
 426 nearest neighbors, as shown in Figure 13. The size of the nearest neighbor can be de-
 427 termined using both definitions of spacing. For both methods, after a slight increase for
 428 the small cloud sizes, the size of the neighboring clouds weakly decreases with cloud size.
 429 However, while both definitions share this weak size-dependence, the feature that most
 430 catches the eye is that the averaged neighbor size is universally larger when using cloud
 431 edge spacing.

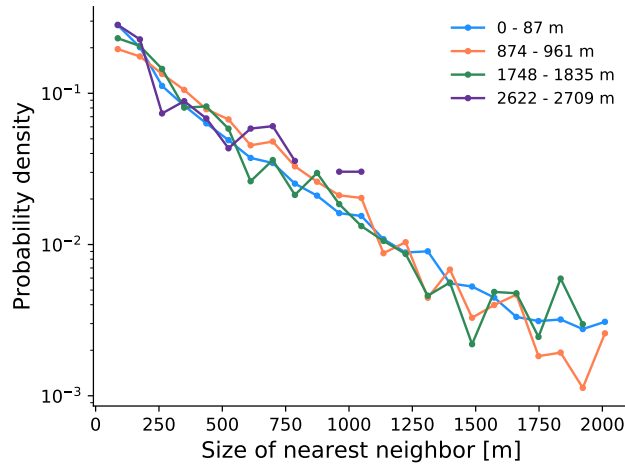


Figure 14. Normalized probability density of the size of the nearest neighbor cloud, for four different size bins.

432 What explains this difference in neighbor size? When edge distancing is used to
 433 determine the nearest neighbor, the radius of the clouds starts to play a role. For big-
 434 ger clouds this matters more than for smaller clouds, because their edge is closer to an
 435 arbitrary cloud of interest compared to their center. As a result, the probability that a
 436 large cloud is closest is bigger when edge distancing is used. This differential impact for
 437 larger clouds also explains the strong impact of edge distancing on the functional depen-
 438 dence of NNS on size, as visible in Figure 10b. For larger clouds their radius makes up
 439 a larger fraction of the center-center distance; as a result, the neighbor spacing reduces
 440 more for larger clouds when switching from center-distancing (Figure 10a) to edge-distancing
 441 (Figure 10b). In effect, this counteracts the logarithmic increase in the center spacing.

442 **4.2 Logarithmic dependence: The role of small clouds**

443 At first glance Figure 13 seems to suggest that large clouds have smaller clouds as
 444 nearest neighbors, and vice versa. However, this dependence should be interpreted with
 445 some caution, because i) the averaging might obscure quite some spread, and ii) the de-
 446 pendence is weak to start with. To gain further insight the probability of having a neigh-
 447 bor of a certain size is investigated, as shown in Figure 14 for four different cloud sizes.
 448 For all cloud sizes considered, the probability of having a small cloud as nearest neigh-
 449 bor is by far the highest (note the logarithmic y-axis). Another interesting feature is that

450 the largest clouds do not even have large clouds as nearest neighbors; smaller clouds are
451 always closer.

452 In combination, these results go some way to explain why the NNS has a logarithmic
453 size-dependence, as shown in Figure 10a. Firstly, it is important to consider that
454 the smallest clouds are by far the most abundant in the field (Figure 9), and are also more
455 or less randomly distributed (Figure 11). This not only means that large clouds have pre-
456 dominantly small clouds as nearest neighbors (Figure 14), but also that the cloud spac-
457 ing that occurs most often in the domain is the equal-size distance of the smallest clouds.
458 In this case this value is about 3.7 km, as marked by the purple circle in Figure 11. As
459 a consequence of the abundance of this spacing, one expects that the NNS of the big-
460 ger clouds can (on average) not be much larger than this value. If this reasoning holds,
461 then the maximum NNS would on average also be 3.7 km, thus more or less acting as
462 a limit value. The purple line shown in Figure 10a indeed seems to act as an upper bound-
463 ary.

464 With the equal-size spacing NNS_{σ} increasing exponentially with size, the picture
465 emerges that the large clusters are swimming in a sea of small clouds. This large spac-
466 ing makes it more likely that smaller clouds (with smaller spacings) are present in be-
467 tween the large clouds, hence the saturation for increasing cloud size. The spatial dis-
468 tribution of the large clouds does not play a role in this, as long as their sample size is
469 large enough and the small clouds indeed dictate the spacing. This argumentation is sum-
470 marized schematically in Figure 15.

471 The existence of an upper limit for the NNS would imply that the NNS will not
472 increase anymore towards very large cloud sizes. Although the logarithmic function fits
473 well to the data at hand, formally such saturation behaviour is not described by a log-
474 arithmic function but an asymptotic one. However, determining in a statistically signif-
475 icant way if the NNS actually saturates requires sampling many more large clouds, much
476 larger than those present in these simulations. Accordingly, answering this question is
477 for now considered future research. This could well be achieved by using an abundance
478 of independent satellite snapshots at high resolutions covering large (ocean-covering) do-
479 mains.

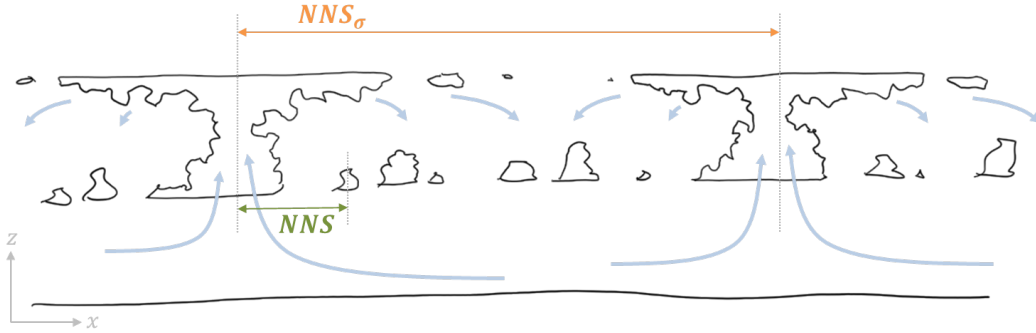


Figure 15. Schematic illustration of the difference in size dependence in the nearest neighbor spacing between clouds of any size (NNS) and between clouds of equal size (NNS_{σ}). In this vertical cross-section the cloud outlines are indicated in black, while the mesoscale cell circulation is shown as thick blue arrows. The two definitions of spacing that are shown apply to the largest cloud size in the domain.

480 **4.3 Exponential dependence: Mesoscale dynamics?**

481 The exponential dependence of the equal-size spacing NNS_{σ} on cloud size is sta-
 482 tistically significant, and also robust for the various definitions of the spacing that are
 483 considered in this study. To our knowledge it has not been reported before, but it is rel-
 484 evant for the representation of convection in weather and climate models. As shown in
 485 Figure 10c, in this case the spacing between clouds increases from about 10km for clouds
 486 of 1km size via 50 km for 2 km-sized clouds to 100km for clouds of 3km. These spacings
 487 are similar to the grid spacings used in global circulation models. Accordingly, they should
 488 be taken into account in the parameterization of convection in the grey zone (Wyngaard,
 489 2004; Honnert et al., 2020), for example in the representation of stochastic effects due
 490 to subsampling (Neggers et al., 2019).

491 The relevance of cloud spacing motivates gaining more insight into what processes
 492 might cause the exponential size-dependence. Convective clouds are the visible parts of
 493 a much larger convective cell, featuring a relatively narrow updraft area and a much wider
 494 area with compensating subsidence that can be either cloudy or cloud free (see Figure
 495 15). Such cells are typically observed in many moist convective regimes, not just fair-
 496 weather cumulus (Shao & Randall, 1996; de Roode et al., 2004). Our results suggest that,
 497 on average, bigger convective clouds need more space around them to form a convective
 498 cell, in a super-linear way. In the mesoscale, the dynamics of such cells markedly changes

499 due to the increasing occurrence of rain. For example, wider and deeper clouds are ob-
500 served when cold pools occur driven by evaporation of rain (Schlemmer & Hohenegger,
501 2014), while precipitation has also been reported to play a role in setting the spatial scale
502 of stratiform convective cells (Zhou et al., 2018; Zhou & Bretherton, 2019). The “flower”
503 type of cloud patterns in the Trades is also associated with such dynamics (Stevens et
504 al., 2019). In general, the interaction of radiation with clouds and water vapor is also
505 thought to play a key process in convective aggregation (Bretherton et al., 2005; Muller
506 & Held, 2012). To summarize, these known impacts on mesoscale dynamics make pre-
507 cipitation and radiative cooling prime candidate processes for controlling the exponen-
508 tially increasing spacing with cloud size. Proving or disproving this hypothesis requires
509 further research.

510 **5 Summary and Conclusions**

511 In this study Large-Eddy Simulations (LES) on super-large-domains are used to
512 investigate how neighbor spacing in cumulus cloud populations depends on cloud size.
513 To this purpose experiments with the ICON LES model of marine shallow cumulus cloud
514 fields in the subtropical Atlantic as observed during the recent NARVAL South campaign
515 were used. Cluster analyses were applied to derive size distributions of both cloud num-
516 ber and cloud spacing. MODIS satellite imagery is first used to test the realism and rep-
517 resentativity of the simulated cloud fields. Despite a slight underestimation of the max-
518 imum cloud size, we find good agreement concerning the shape of the number distribu-
519 tion. A multitude of instantaneous snapshots from the simulation are then used to di-
520 agnose the cloud Nearest Neighbor Spacing (NNS), of which four possible definitions are
521 considered. We find that in general the NNS increases with cloud size, a result which is
522 in line with the findings of previous observational studies. However, the functional form
523 of the size-dependence strongly depends on the exact definition of the NNS. Its classic
524 definition, the spacing between clouds of any size, carries a well-defined logarithmic size-
525 dependence. In contrast, only considering clouds of equal size yields cloud spacings that
526 are larger but also carry a strong exponential size-dependence. Deeper investigation into
527 this behavior reveals that the abundance of closely-spaced small clouds in the popula-
528 tion is responsible for the logarithmic dependence. The exponential dependence is spec-
529 ulated to express the role of mesoscale dynamics in controlling the width of the convec-
530 tive cells of which the cumulus clouds are the visible parts.

531 The results obtained in this study are relevant for ongoing research into the spa-
532 tial organization and aggregation of convection and its impact on climate (Wing, 2019).
533 It has long been understood that cloud spacing is a key ingredient in this problem, as
534 testified by the various metrics for the degree of spatial organization that have been pro-
535 posed that are formulated in terms of the neighbor spacing (Weger et al., 1992; Tomp-
536 kins & Semie, 2017). Most of these metrics depend on the spacing between clouds of any
537 size. However, the equal-size spacing as investigated in this study could also be used to
538 this purpose, yielding an alternative organizational metric that expresses different as-
539 pects of this phenomenon. A recent example is the B_{org} metric as proposed by Neggers
540 et al. (2019), which exclusively relies on equal-size cloud spacing (NNS_{σ}) and expresses
541 the degree of organization per cloud size. In the context of understanding cloud-climate
542 feedbacks the exponential spacing might also be relevant, as it affects the impact of such
543 cloud fields on radiation, in particular at low solar inclination angles.

544 The results of this study also have a bearing on the parameterization of convec-
545 tion in the grey zone (Wyngaard, 2004; Honnert et al., 2020). For example, the stochas-
546 tic effects of subsampling on the cloud size distribution to be parameterized can be cap-
547 tured by using the neighbor spacing (Neggers et al., 2019). The functional form in the
548 size-dependence of the cloud spacing can thus inform the further development of con-
549 vection schemes based on cloud size distributions (Neggers, 2015; Sakradzija et al., 2016;
550 Hagos et al., 2018). Through metrics relying on the neighbor spacing, constants of pro-
551 portionality in such schemes could be constrained against observed and simulated cloud
552 fields, for example using machine learning techniques.

553 This study has several limitations which could inspire future research efforts. Firstly,
554 only relatively homogeneous conditions were considered, in order to focus on internal spa-
555 tial organization in a cloud population. But heterogeneity in the larger-scale flow and
556 surface can also affect the cloud spacing. Gaining insight into these impacts is needed
557 to test the general applicability of the size dependence in cloud spacing as reported in
558 this study. Secondly, the domain size could still artificially limit the maximum cloud size,
559 which motivates considering even larger domain simulations. Another simplification in
560 the experimental configuration is the use of 1D radiation in the simulation, which ignores
561 three-dimensional effects that can change cloud alignment and spacing (Jakub & Mayer,
562 2017). Finally, we only applied our spacing analysis to simulated cloud fields. To seek
563 observational support for the obtained results, an obvious next step would be to derive

564 cloud spacing from multiple high-resolution satellite images. Such data is increasingly
 565 available, and is actively being used to investigate mesoscale spatial structures in low level
 566 cloud fields (Bony et al., 2020).

567 **Acknowledgments**

568 This research is supported by the SFB-TR32 'Patterns in soil-vegetation-atmosphere sys-
 569 tems: monitoring, modelling and data assimilation', funded by the German Science Foun-
 570 dation (DFG). The authors want to thank Matthias Brueck from the Max-Planck-Institut
 571 für Meteorologie in Hamburg (MPI-H) who performed the ICON simulations in the scope
 572 of the HD(CP)² project. The NARVAL I data used in this publication is made available
 573 through the German Aerospace Center (DLR). NARVAL was funded with support of
 574 the Max Planck Society, the German Research Foundation (DFG, project HALO-SPP
 575 1294), the European Research Council (ERC), the German Meteorological Weather Ser-
 576 vice (DWD) and DLR. The simulation data used in this study is available at the follow-
 577 ing website: <https://doi.org/10.5281/zenodo.3531556>.

578 **References**

- 579 Ali, K. (1998). Spatial distribution of convective clouds in north India. *Atmospheric*
 580 *Research*, *49*(1), 1 - 10. Retrieved from [http://www.sciencedirect.com/](http://www.sciencedirect.com/science/article/pii/S0169809598000702)
 581 [science/article/pii/S0169809598000702](http://www.sciencedirect.com/science/article/pii/S0169809598000702) doi: [https://doi.org/10.1016/](https://doi.org/10.1016/S0169-8095(98)00070-2)
 582 [S0169-8095\(98\)00070-2](https://doi.org/10.1016/S0169-8095(98)00070-2)
- 583 Baldauf, M., Seifert, A., Förstner, J., Majewski, D., Raschendorfer, M., & Rein-
 584 hardt, T. (2011). Operational convective-scale numerical weather prediction
 585 with the COSMO model: Description and sensitivities. *Monthly Weather*
 586 *Review*, *139*(12), 3887 - 3905. doi: [10.1175/mwr-d-10-05013.1](https://doi.org/10.1175/mwr-d-10-05013.1)
- 587 Bony, S., & Dufresne, J.-L. (2005). Marine boundary layer clouds at the heart of
 588 tropical cloud feedback uncertainties in climate models. *Geophysical Research*
 589 *Letters*, *32*(20). Retrieved from [https://agupubs.onlinelibrary.wiley](https://agupubs.onlinelibrary.wiley.com/doi/abs/10.1029/2005GL023851)
 590 [.com/doi/abs/10.1029/2005GL023851](https://agupubs.onlinelibrary.wiley.com/doi/abs/10.1029/2005GL023851) doi: [10.1029/2005GL023851](https://doi.org/10.1029/2005GL023851)
- 591 Bony, S., Schulz, H., Vial, J., & Stevens, B. (2020). Sugar, gravel, fish, and flow-
 592 ers: Dependence of mesoscale patterns of trade-wind clouds on environ-
 593 mental conditions. *Geophysical Research Letters*, *47*(7), e2019GL085988.
 594 Retrieved from <https://agupubs.onlinelibrary.wiley.com/doi/abs/>

- 595 10.1029/2019GL085988 (e2019GL085988 10.1029/2019GL085988) doi:
 596 10.1029/2019GL085988
- 597 Brast, M., Schemann, V., & Neggers, R. A. J. (2018). Investigating the scale
 598 adaptivity of a size-filtered mass flux parameterization in the gray zone
 599 of shallow cumulus convection. *J. Atmos. Sci.*, *75*(4), 1195–1214. doi:
 600 10.1175/jas-d-17-0231.1
- 601 Bretherton, C. S., & Blossey, P. N. (2017). Understanding mesoscale aggregation of
 602 shallow cumulus convection using large-eddy simulation. *J. Adv. Model Earth
 603 Syst.*, *9*(8), 2798–2821. doi: 10.1002/2017ms000981
- 604 Bretherton, C. S., Blossey, P. N., & Khairoutdinov, M. (2005). An energy-balance
 605 analysis of deep convective self-aggregation above uniform SST. *J. Atmos. Sci.*,
 606 *62*(12), 4273–4292. doi: 10.1175/jas3614.1
- 607 Dawe, J., & Austin, P. (2013). Direct entrainment and detrainment rate distribu-
 608 tions of individual shallow cumulus clouds in an LES. *Atmos. Chem. Phys.*, *13*,
 609 7795–7811. doi: 10.5194/acp-13-7795-2013
- 610 de Roode, S. R., Duynkerke, P. G., & Jonker, H. J. J. (2004). Large-eddy simula-
 611 tion: How large is large enough? *J. Atmos. Sci.*, *61*(4), 403–421. doi: 10.1175/
 612 1520-0469(2004)061<0403:lshlil>2.0.co;2
- 613 Hagos, S., Feng, Z., Plant, R. S., Houze Jr., R. A., & Xiao, H. (2018). A stochas-
 614 tic framework for modeling the population dynamics of convective clouds.
 615 *Journal of Advances in Modeling Earth Systems*, *10*(2), 448–465. Retrieved
 616 from [https://agupubs.onlinelibrary.wiley.com/doi/abs/10.1002/](https://agupubs.onlinelibrary.wiley.com/doi/abs/10.1002/2017MS001214)
 617 [2017MS001214](https://agupubs.onlinelibrary.wiley.com/doi/abs/10.1002/2017MS001214) doi: 10.1002/2017MS001214
- 618 Heinze, R., Dipankar, A., Henken, C. C., et al. (2017). Large-eddy simulations over
 619 Germany using ICON: a comprehensive evaluation. *Q. J. Roy. Meteorol. Soc.*,
 620 *143*(702), 69–100. doi: 10.1002/qj.2947
- 621 Honnert, R., Efstathiou, G. A., Beare, R. J., Ito, J., Lock, A., Neggers, R., . . . Zhou,
 622 B. (2020). The atmospheric boundary layer and the “gray zone” of turbulence:
 623 A critical review. *Journal of Geophysical Research: Atmospheres*, *n/a*(n/a),
 624 e2019JD030317. doi: 10.1029/2019JD030317
- 625 Jacob, M., Ament, F., Gutleben, M., Konow, H., Mech, M., Wirth, M., & Crewell,
 626 S. (2019). Investigating the liquid water path over the tropical atlantic with
 627 synergistic airborne measurements. *Atmospheric Measurement Techniques*

- 628 *Discussions*, 1–27. doi: 10.5194/amt-2019-18
- 629 Jakub, F., & Mayer, B. (2017). The role of 1-D and 3-D radiative heating in
 630 the organization of shallow cumulus convection and the formation of cloud
 631 streets. *Atmospheric Chemistry and Physics*, 17(21), 13317–13327. doi:
 632 10.5194/acp-17-13317-2017
- 633 Joseph, J. H., & Cahalan, R. F. (1990). Nearest neighbor spacing of fair
 634 weather cumulus clouds. *J. Appl. Meteorol.*, 29(8), 793–805. doi: 10.1175/
 635 1520-0450(1990)029<0793:NNSOFW>2.0.CO;2
- 636 Klepp, C., Ament, F., Bakan, S., Hirsch, L., & Stevens, B. (2014). The NARVAL
 637 campaign report. *Berichte zur Erdsystemforschung / Max-Planck-Institut für*
 638 *Meteorologie*, 164.
- 639 Klocke, D., Brueck, M., Hohenegger, C., & Stevens, B. (2017). Rediscovery of the
 640 doldrums in storm-resolving simulations over the tropical Atlantic. *Nature*
 641 *Geosci.*, 10(12), 891–896. doi: 10.1038/s41561-017-0005-4
- 642 Mlawer, E. J., Taubman, S. J., Brown, P. D., Iacono, M. J., & Clough, S. A. (1997).
 643 Radiative transfer for inhomogeneous atmospheres: RRTM, a validated
 644 correlated-k model for the longwave. *Journal of Geophysical Research: At-*
 645 *mospheres*, 102(D14), 16663 - 16682. doi: 10.1029/97jd00237
- 646 Muller, C. J., & Held, I. M. (2012). Detailed Investigation of the Self-Aggregation
 647 of Convection in Cloud-Resolving Simulations. *Journal of the Atmospheric Sci-*
 648 *ences*, 69(8), 2551-2565. Retrieved from [https://doi.org/10.1175/JAS-D-11-](https://doi.org/10.1175/JAS-D-11-0257.1)
 649 [0257.1](https://doi.org/10.1175/JAS-D-11-0257.1) doi: 10.1175/JAS-D-11-0257.1
- 650 Nair, U. S., Weger, R. C., Kuo, K. S., & Welch, R. M. (1998). Clustering, ran-
 651 domness, and regularity in cloud fields: 5. the nature of regular cumulus
 652 cloud fields. *J. Geophys. Res.: Atmospheres*, 103(D10), 11363–11380. doi:
 653 10.1029/98jd00088
- 654 Nam, C., Bony, S., Dufresne, J.-L., & Chepfer, H. (2012). The ‘too few, too bright’
 655 tropical low-cloud problem in CMIP5 models. *Geophysical Research Letters*,
 656 39(21). Retrieved from [https://agupubs.onlinelibrary.wiley.com/doi/](https://agupubs.onlinelibrary.wiley.com/doi/abs/10.1029/2012GL053421)
 657 [abs/10.1029/2012GL053421](https://agupubs.onlinelibrary.wiley.com/doi/abs/10.1029/2012GL053421) doi: 10.1029/2012GL053421
- 658 Narenpitak, P., Bretherton, C. S., & Khairoutdinov, M. F. (2017). Cloud and
 659 circulation feedbacks in a near-global aquaplanet cloud-resolving model. *Jour-*
 660 *nal of Advances in Modeling Earth Systems*, 9(2), 1069-1090. Retrieved

- 661 from <https://agupubs.onlinelibrary.wiley.com/doi/abs/10.1002/>
 662 2016MS000872 doi: 10.1002/2016MS000872
- 663 Naumann, A. K., & Kiemle, C. (2020). The vertical Structure and spatial Variabil-
 664 ity of lower tropospheric Water Vapor and Clouds in the Trades. *Atmospheric*
 665 *Chemistry and Physics*. doi: 10.5194/acp-20-6129-2020
- 666 Neggers, R. A. J. (2015). Exploring bin-macrophysics models for moist convective
 667 transport and clouds. *J. Adv. Model Earth Syst.*, 7(4), 2079–2104. doi: 10
 668 .1002/2015MS000502
- 669 Neggers, R. A. J., Griewank, P. J., & Heus, T. (2019). Powerlaw scaling in the
 670 internal variability of cumulus cloud size distributions due to subsampling and
 671 spatial organization. *J. Atmos. Sci.* doi: 10.1175/jas-d-18-0194.1
- 672 Neggers, R. A. J., Jonker, H. J. J., & Siebesma, A. P. (2003). Size statistics of
 673 cumulus cloud populations in large-eddy simulations. *J. Atmos. Sci.*, 60(8),
 674 1060–1074. doi: 10.1175/1520-0469(2003)60<1060:SSOCCP>2.0.CO;2
- 675 Norris, J. R. (1998). Low Cloud Type over the Ocean from Surface Observations.
 676 Part II: Geographical and Seasonal Variations. *Journal of Climate*, 11(3), 383-
 677 403. Retrieved from [https://doi.org/10.1175/1520-0442\(1998\)011<0383:](https://doi.org/10.1175/1520-0442(1998)011<0383:LCTOTO>2.0.CO;2)
 678 [LCTOTO>2.0.CO;2](https://doi.org/10.1175/1520-0442(1998)011<0383:LCTOTO>2.0.CO;2) doi: 10.1175/1520-0442(1998)011<0383:LCTOTO>2.0.CO;
 679 2
- 680 Nuijens, L., Serikov, I., Hirsch, L., Lonitz, K., & Stevens, B. (2014). The distribu-
 681 tion and variability of low-level cloud in the north atlantic trades. *Q. J. Roy.*
 682 *Meteorol. Soc.*, 140(684), 2364–2374. doi: 10.1002/qj.2307
- 683 Plank, V. G. (1969). The size distribution of cumulus clouds in representa-
 684 tive Florida populations. *J. Appl. Meteor.*, 8(1), 46–67. doi: 10.1175/
 685 1520-0450(1969)008<0046:TSDOCC>2.0.CO;2
- 686 Quinn, K. M., & Neelin, J. D. (2017). Distributions of Tropical Precipitation Clus-
 687 ter Power and Their Changes under Global Warming. Part I: Observational
 688 Baseline and Comparison to a High-Resolution Atmospheric Model. *Journal*
 689 *of Climate*, 30(20), 8033-8044. Retrieved from [https://doi.org/10.1175/](https://doi.org/10.1175/JCLI-D-16-0683.1)
 690 [JCLI-D-16-0683.1](https://doi.org/10.1175/JCLI-D-16-0683.1) doi: 10.1175/JCLI-D-16-0683.1
- 691 Reilly, S., Gesso, S. D., & Neggers, R. (2019). Configuring LES in sparsely sampled
 692 areas in the subtropical atlantic. *Journal of Applied Meteorology and Climatol-*
 693 *ogy, submitted.*

- 694 Rieck, M., Hohenegger, C., & van Heerwaarden, C. C. (2014). The influence of land
695 surface heterogeneities on cloud size development. *Mon. Wea. Rev.*, *142*(10),
696 3830–3846. doi: 10.1175/MWR-D-13-00354.1
- 697 Sakradzija, M., Seifert, A., & Dipankar, A. (2016). A stochastic scale-aware param-
698 eterization of shallow cumulus convection across the convective gray zone. *J.*
699 *Adv. Model Earth Syst.*, *8*(2), 786–812. doi: 10.1002/2016ms000634
- 700 Schikuta, E. (1996). Grid-clustering: an efficient hierarchical clustering method for
701 very large data sets. *Proceedings of the 13th International Conference on Pat-*
702 *tern Recognition*, *2*, 101-105.
- 703 Schlemmer, L., & Hohenegger, C. (2014). The Formation of Wider and Deeper
704 Clouds as a Result of Cold-Pool Dynamics. *Journal of the Atmospheric*
705 *Sciences*, *71*(8), 2842-2858. Retrieved from [https://doi.org/10.1175/](https://doi.org/10.1175/JAS-D-13-0170.1)
706 [JAS-D-13-0170.1](https://doi.org/10.1175/JAS-D-13-0170.1) doi: 10.1175/JAS-D-13-0170.1
- 707 Schnitt, S., Orlandi, E., Mech, M., Ehrlich, A., & Crewell, S. (2017). Characteriza-
708 tion of Water Vapor and Clouds During the Next-Generation Aircraft Remote
709 Sensing for Validation (NARVAL) South Studies. *IEEE Journal of Selected*
710 *Topics in Applied Earth Observations and Remote Sensing*, *10*(7), 3114–3124.
711 doi: 10.1109/jstars.2017.2687943
- 712 Senf, F., Klocke, D., & Brueck, M. (2018). Size-resolved evaluation of simulated
713 deep tropical convection. *Mon. Wea. Rev.*, *146*(7), 2161–2182. doi: 10.1175/
714 [mwr-d-17-0378.1](https://doi.org/10.1175/mwr-d-17-0378.1)
- 715 Sengupta, S., Welch, R., Navar, M., Berendes, T., & Chen, D. (1990). Cu-
716 mulus cloud field morphology and spatial patterns derived from high spa-
717 tial resolution Landsat imagery. *J. Appl. Meteorol.*, *29*(1245-1267). doi:
718 [10.1175/1520-0450\(1990\)029<1245:CCFMAS>2.0.CO;2](https://doi.org/10.1175/1520-0450(1990)029<1245:CCFMAS>2.0.CO;2)
- 719 Shao, Q., & Randall, D. A. (1996). Closed Mesoscale Cellular Convection Driven by
720 Cloud-Top Radiative Cooling. *Journal of the Atmospheric Sciences*, *53*(15),
721 2144-2165. Retrieved from [https://doi.org/10.1175/1520-0469\(1996\)](https://doi.org/10.1175/1520-0469(1996)053<2144:CMCCDB>2.0.CO;2)
722 [053<2144:CMCCDB>2.0.CO;2](https://doi.org/10.1175/1520-0469(1996)053<2144:CMCCDB>2.0.CO;2) doi: 10.1175/1520-0469(1996)053<2144:
723 [CMCCDB>2.0.CO;2](https://doi.org/10.1175/1520-0469(1996)053<2144:CMCCDB>2.0.CO;2)
- 724 Sherwood, S., Bony, S., & Dufresne, J. (2014). Spread in model climate sensitivity
725 traced to atmospheric convective mixing. *Nature*, *505*, 37-42. doi: 10.1038/
726 [nature12829](https://doi.org/10.1038/nature12829)

- 727 Stevens, B., Ackerman, A. S., Albrecht, B. A., Brown, A. R., Chlond, A., Cuxart,
 728 J., ... Stevens, D. E. (2001). Simulations of trade wind cumuli under
 729 a strong inversion. *Journal of the Atmospheric Sciences*, 58(14), 1870 -
 730 1891. Retrieved from [https://journals.ametsoc.org/view/journals/
 731 atasc/58/14/1520-0469_2001_058_1870_sotwcu.2.0.co_2.xml](https://journals.ametsoc.org/view/journals/atasc/58/14/1520-0469_2001_058_1870_sotwcu.2.0.co_2.xml) doi:
 732 10.1175/1520-0469(2001)058<1870:SOTWCU>2.0.CO;2
- 733 Stevens, B., Ament, F., Bony, S., Crewell, S., Ewald, F., Gross, S., ... Zinner, T.
 734 (2019). A High-Altitude Long-Range Aircraft Configured as a Cloud Obser-
 735 vatory: The NARVAL Expeditions. *Bulletin of the American Meteorological
 736 Society*, 100(6), 1061-1077. Retrieved from [https://doi.org/10.1175/
 737 BAMS-D-18-0198.1](https://doi.org/10.1175/BAMS-D-18-0198.1) doi: 10.1175/BAMS-D-18-0198.1
- 738 Tompkins, A. M., & Semie, A. G. (2017). Organization of tropical convection in low
 739 vertical wind shears: Role of updraft entrainment. *J. Adv. Model Earth Syst.*,
 740 9(2), 1046–1068. doi: 10.1002/2016ms000802
- 741 van Laar, T. W., Schemann, V., & Neggers, R. A. J. (2019). Investigating
 742 the diurnal evolution of the cloud size distribution of continental cumu-
 743 lus convection using multiday LES. *J. Atmos. Sci.*, 76(3), 729–747. doi:
 744 10.1175/jas-d-18-0084.1
- 745 vanZanten, M. C., Stevens, B., Nuijens, L., Siebesma, A. P., Ackerman, A. S., Bur-
 746 net, F., ... Wyszogrodzki, A. (2011). Controls on precipitation and cloudi-
 747 ness in simulations of trade-wind cumulus as observed during rico. *Journal
 748 of Advances in Modeling Earth Systems*, 3(2). Retrieved from [https://
 749 agupubs.onlinelibrary.wiley.com/doi/abs/10.1029/2011MS000056](https://agupubs.onlinelibrary.wiley.com/doi/abs/10.1029/2011MS000056) doi:
 750 <https://doi.org/10.1029/2011MS000056>
- 751 Vial, J., Bony, S., Dufresne, J.-L., & Roehrig, R. (2016). Coupling between lower-
 752 tropospheric convective mixing and low-level clouds: Physical mechanisms and
 753 dependence on convection scheme. *J. Adv. Model Earth Syst.*, 8(4), 1892–1911.
 754 doi: 10.1002/2016MS000740
- 755 Vial, J., Vogel, R., Bony, S., Stevens, B., Winker, D. M., Cai, X., ... Brogniez,
 756 H. (2019). A new look at the daily cycle of trade wind cumuli. *Jour-
 757 nal of Advances in Modeling Earth Systems*, 11(10), 3148-3166. Retrieved
 758 from [https://agupubs.onlinelibrary.wiley.com/doi/abs/10.1029/
 759 2019MS001746](https://agupubs.onlinelibrary.wiley.com/doi/abs/10.1029/2019MS001746) doi: 10.1029/2019MS001746

- 760 Weger, R. C., Lee, J., & Welch, R. M. (1993). Clustering, randomness, and regular-
 761 ity in cloud fields: 3. the nature and distribution of clusters. *J. Geophys. Res.*,
 762 98(D10), 18449-18463.
- 763 Weger, R. C., Lee, J., Zhu, T., & Welch, R. M. (1992). Clustering, randomness
 764 and regularity in cloud fields: 1. theoretical considerations. *J. Geophys. Res.*,
 765 97(D18), 20519. doi: 10.1029/92jd02038
- 766 Wing, A. A. (2019). Self-aggregation of deep convection and its implications for cli-
 767 mate. *Current Climate Change Reports*, 5(1), 1–11. doi: 10.1007/s40641-019
 768 -00120-3
- 769 Wing, A. A., & Cronin, T. W. (2015). Self-aggregation of convection in long channel
 770 geometry. *Q. J. Roy. Meteorol. Soc.*, 142(694), 1–15. doi: 10.1002/qj.2628
- 771 Wyngaard, J. C. (2004). Toward numerical modeling in the 'Terra Incognita'.
 772 *J. Atmos. Sci.*, 61(14), 1816–1826. doi: 10.1175/1520-0469(2004)061<1816:
 773 TNMITT>2.0.CO;2
- 774 Zängl, G., Reinert, D., Rípodas, P., & Baldauf, M. (2014). The ICON (ICOsahedral
 775 non-hydrostatic) modelling framework of DWD and MPI-m: Description of the
 776 non-hydrostatic dynamical core. *Q. J. Roy. Meteorol. Soc.*, 141(687), 563–579.
 777 doi: 10.1002/qj.2378
- 778 Zhang, M., Bretherton, C. S., Blossey, P. N., et al. (2013). CGILS: Results from the
 779 first phase of an international project to understand the physical mechanisms
 780 of low cloud feedbacks in single column models. *J. Adv. Model Earth Syst.*,
 781 5(4), 826–842. doi: 10.1002/2013MS000246
- 782 Zhang, Y., Klein, S. A., Fan, J., et al. (2017). Large-eddy simulation of shal-
 783 low cumulus over land: A composite case based on arm long-term ob-
 784 servations at its southern great plains site. *J. Atmos. Sci.*, 74. doi:
 785 <https://doi.org/10.1175/JAS-D-16-0317.1>
- 786 Zhou, X., Ackerman, A. S., Fridlind, A. M., & Kollias, P. (2018). Simula-
 787 tion of Mesoscale Cellular Convection in Marine Stratocumulus. Part I:
 788 Drizzling Conditions. *Journal of the Atmospheric Sciences*, 75(1), 257-
 789 274. Retrieved from <https://doi.org/10.1175/JAS-D-17-0070.1> doi:
 790 10.1175/JAS-D-17-0070.1
- 791 Zhou, X., & Bretherton, C. S. (2019). Simulation of mesoscale cellular convec-
 792 tion in marine stratocumulus: 2. nondrizzling conditions. *Journal of Ad-*

793 *vances in Modeling Earth Systems*, 11(1), 3-18. Retrieved from [https://](https://agupubs.onlinelibrary.wiley.com/doi/abs/10.1029/2018MS001448)
794 agupubs.onlinelibrary.wiley.com/doi/abs/10.1029/2018MS001448 doi:
795 10.1029/2018MS001448
796 Zhu, T., Lee, J., Weger, R. C., & Welch, R. M. (1992). Clustering, randomness, and
797 regularity in cloud fields: 2. cumulus cloud fields. *J. Geophys. Res.*, 97(D18),
798 20537. doi: 10.1029/92jd02022